TIaRA *TESS* 1: estimating exoplanet yields from Years 1 and 3 SPOC light curves

Toby Rodel [1,2,3]★ Daniel Bayliss [1,2] Samuel Gill [1,2] and Faith Hawthorn [1,2]

[1] *Department of Physics, University of Warwick, Gibbet Hill Road, Coventry CV4 7AL, UK*
[2] *Centre for Exoplanets and Habitability, University of Warwick, Gibbet Hill Road, Coventry CV4 7AL, UK*
[3] *Astrophysics Research Centre, School of Mathematics and Physics, Queen's University Belfast, Belfast BT7 1NN, UK*

ABSTRACT

We present a study of the detection efficiency for the *TESS* mission, focusing on the yield of longer period transiting exoplanets ($P > 25$ d). We created the Transit Investigation and Recoverability Application (TIaRA) pipeline to use real *TESS* data with injected transits to create sensitivity maps which we combine with occurrence rates derived from *Kepler*. This allows us to predict longer period exoplanet yields, which will help design follow-up photometric and spectroscopic programs, such as the *NGTS* (*Next Generation Transit Survey*) Monotransit Program. For the *TESS* Years 1 and 3 SPOC (Science Processing Operations Centre) FFI (Full Frame Image) light curves, we find 2271^{+241}_{-138} exoplanets should be detectable around AFGKM dwarf host stars. We find 215^{+37}_{-23} exoplanets should be detected from single-transit events or 'monotransits'. An additional 113^{+22}_{-13} detections should result from 'biennial duotransit' events with one transit in Year 1 and a second in Year 3. We also find that K dwarf stars yield the most detections by *TESS* per star observed. When comparing our results to the TOI (*TESS* objects of interest) catalogue, we find our predictions agree within 1σ of the number of discovered systems with periods between 0.78 and 6.25 d and agree to 2σ for periods between 6.25 and 25 d. Beyond periods of 25 d, we predict 403^{+64}_{-38} detections, which is three times as many detections as there are in the TOI catalogue with $>3\sigma$ confidence. This indicates a significant number of long-period planets yet to be discovered from *TESS* data as monotransits or biennial duotransits.

Key words: planets and satellites: detection.

1 INTRODUCTION

Transiting exoplanets are of exceptional scientific importance as they allow for many parameters of a planetary system to be characterized. Transit detections themselves allow for the orbital period and radius ratio of a planet and its host to be constrained (Winn 2014). If the host star is sufficiently bright, spectroscopic radial velocity (RV) measurements can be used to constrain the planetary mass. These can be combined with transit radius measurements to constrain the planetary density and make inferences about composition and internal structure. The brightest host stars also permit atmospheric characterisation of planets via transmission spectroscopy (e.g. Charbonneau et al. 2002; Madhusudhan et al. 2014a; Kempton et al. 2018; Kreidberg 2018; Madhusudhan 2019).

Discoveries from transit surveys are biased towards shorter-period planets. Shorter-period planets have a greater geometric probability of transit (Winn 2014) and transit more frequently within any given monitoring campaign, resulting in an increase in the signal-to-noise ratio (SNR) of the transit signal. Despite this; longer period planet discoveries are valuable.

Longer period planets yield insights into planet formation and migration mechanisms. At the extremely small orbital separation of

planets with $P < 10$ d star–planet interactions may have a significant effect on dynamical evolution (Valsecchi et al. 2015). This leads to very reduced eccentricities (Albrecht et al. 2012; Winn 2014), effectively removing any trace of past dynamical interactions from the planet's present-day orbit. Planets with longer orbital periods have larger orbital separations and as such experience weaker star–planet interactions, retaining more information on past dynamical interactions. Giant planets on extremely short periods (i.e. 'hot-Jupiters') and those on longer periods ('warm-Jupiters') have been shown to exhibit differences in their distributions of orbital eccentricity (Dong et al. 2021) and the number of close orbital companions (Huang, Wu & Triaud 2016). This indicates that giant planets with orbital periods longer than 10 d may experience different migration pathways compared with short-period giant planets (Wu & Lithwick 2011; Petrovich 2014; Mustill, Davies & Johansen 2017). Furthermore, Rossiter–McLaughlin (RM; McLaughlin 1924; Rossiter 1924) measurements of orbital obliquity allow further constraining of possible migration mechanisms in the planet's history (Triaud 2018). Already, Rice et al. (2022) have found a trend towards more aligned obliquities in some warm-Jupiters compared to hot-Jupiters lthough the number of well-studied warm-Jupiters is comparatively fewer.

Additionally, short-period planets experience a greater level of atmospheric mass loss than those on longer periods (Owen 2019), meaning longer period planets will retain more of their
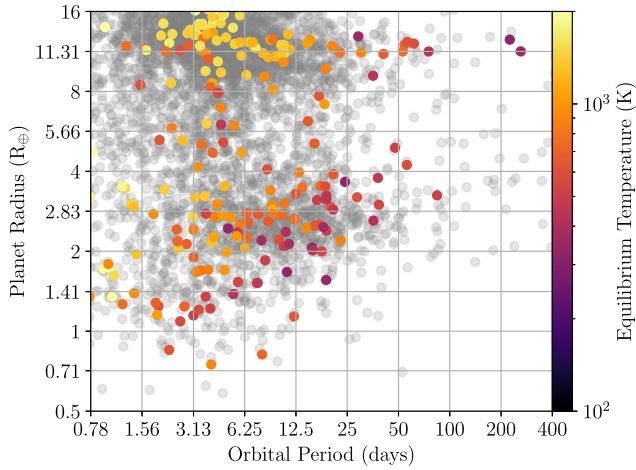
★ E-mail: trodel01@qub.ac.uk

Figure 1. The *TESS* planet sample. Full sample of TOI are shown in grey and confirmed TOIs are coloured according to their equilibrium temperature. The full 5910 TOIs consist of the *TESS* project candidate list excluding those flagged as false positives. The 273 confirmed *TESS* planets include all published and confirmed exoplanets from *TESS* with fully constrained, masses, radii, and orbital periods. Both data sets were downloaded from the NASA exoplanet archive (Akeson et al. 2013) on 2023 November 23.

atmospheres. This makes long-period planets promising targets for atmospheric studies to probe cooler atmospheres that have undergone less photo-evaporation and to gain an accurate understanding of their formation (Öberg, Murray-Clay & Bergin 2011; Madhusudhan, Amin & Kennedy 2014b). However, in spite of their promise, longer period cooler planets are more difficult targets for transmission spectroscopy than closer-in hotter planets due to their generally smaller atmospheric scale height (Kempton et al. 2018).

Long-period planets also offer important targets in the search for exomoons and exorings, which have not yet been detected but are theoretically detectable around giant transiting planets (Barnes & Fortney 2004; Kipping, Fossey & Campanella 2009; Simon et al. 2012; Aizawa et al. 2017). Exomoons and exorings are predicted to be more stable and thus likelier to exist around longer period planets with greater orbital separations (Barnes & O'Brien 2002; Barnes & Fortney 2004; Cassidy et al. 2009; Dobos et al. 2021; Makarov & Efroimsky 2023).

Since 2018, the Transiting Exoplanet Survey Satellite (*TESS*; Ricker et al. 2014) has been performing an all-sky survey searching for transiting exoplanets around bright host stars. One of the primary science goals is to find nearby planets amenable to atmospheric characterization (Ricker et al. 2014; Kempton et al. 2018). *TESS* observes each $24° \times 96°$ sector of sky for 27 d at a time, although overlap of some regions between sectors mean that the observation baselines for some targets will be >300 d near the Ecliptic poles in the continuous viewing zone (CVZ; Ricker et al. 2014). However, in the first year of *TESS* ≈ 75 per cent of target stars were only observed in a single sector which means that longer period planets are likely to only be observed as a single transit. Fig. 1 shows the population of *TESS* planet detections both confirmed and unconfirmed, showing the relative lack of longer period planets. Although such single-transiting candidates are harder to detect, it is not impossible and the ability of *TESS* to do so has been studied previously in Cooke et al. (2018), Cooke, Pollacco & Bayliss (2019), and Villanueva, Dragomir & Gaudi (2019). Additionally, a number of long-period transiting planets have been discovered via monotransits from the

K2 (Howell et al. 2014) mission (e.g; Vanderburg et al. 2015, 2016; Giles et al. 2018; Kruse et al. 2019).

Planets discovered from a single transit ('monotransits') do not have constrained periods and require follow-up observations to rule out false positive scenarios and constrain their periods. Such observations can be performed using photometry or spectroscopic RV measurements.

Photometric observations can be used to detect additional transit events, which will either determine the period uniquely, or provide a discrete set of aliases (e.g; Gill et al. 2020). This is one of the science goals of the *Next Generation Transit Survey* (*NGTS*; Wheatley et al. 2018) monotransit working group, which uses the 12-telescope *NGTS* facility in Paranal, Chile to monitor *TESS* monotransit candidates that display transit events with depths 1000 ppm or greater (Bayliss et al. 2020). This program has already successfully confirmed 'monotransits' from *TESS* data (e.g. Gill et al. 2020; Lendl et al. 2020; Grieves et al. 2022; Ulmer-Moll et al. 2022). The *TESS* single-transit planet group has also been following up monotransits using a global network of small telescopes (Dragomir et al. 2023).

For shallower *TESS* monotransits (<1000 ppm) usually associated with smaller planets it is extremely difficult to detect additional transits from the ground. In these cases space facilities such as *CHEOPS* (Benz et al. 2021) can be used to detect further transits, for example (Osborn et al. 2023; Tuson et al. 2023; Ulmer-Moll et al. 2023).

Spectroscopic monitoring of monotransits can also determine the true period of a planet candidate and rule out some eclipsing binary stars which display very large RV variations (e.g; Dragomir et al. 2019; Eberhardt et al. 2022; Ulmer-Moll et al. 2022). However, this requires long-term spectroscopic monitoring of candidates with high-resolution instruments. Such spectrographs have to be mounted on large telescopes for which observing time is limited.

Given the large-effort and hundreds of hours of telescope time involved with such follow-up efforts, it is vital to inform these efforts with up-to-date understanding of the sensitivity of *TESS* to monotransit events and the expected yield of monotransits from the mission.

Previous studies of yields from the *TESS* mission have largely focused on multi-event signals. Prior to the launch of *TESS*, yield estimates were predicted in Sullivan et al. (2015) and Bouma et al. (2017) based on the expected performance of the mission given in Ricker et al. (2014).

Around the time that *TESS* was launched there were several studies that estimated the potential yields from the *TESS* mission, including: Barclay, Pepper & Quintana (2018), Huang et al. (2018), Muirhead et al. (2018), and Ballard (2019). These studies were still largely based on the expected performance of the *TESS* mission as the data from the mission was only just becoming available. More recently, Kunimoto et al. (2022) have revised the yield estimates based on the performance of *TESS* in its primary and first extended mission. All of these studies were largely focused on planet discoveries from two or more transits.

The studies of Cooke et al. (2018) and Villanueva et al. (2019) were specifically focused on the expected yield of monotransits from *TESS*. These studies were mostly based on the expected performance of *TESS* from Ricker et al. (2014) due to the relative lack of *TESS* data available at the time of publication shortly after *TESS* had launched. Cooke et al. (2019) provided an update to the yields from Cooke et al. (2018) using the performance of the *TESS* primary mission and estimating the yield when *TESS* revisited the southern ecliptic in Year 3 during its first extended mission. All of these studies found

that a significant number of long-period planets will be detectable in *TESS* light curves as monotransits.

In this study, we use the custom-made Transit Investigation and Recoverability Application (TIARA) pipeline to create sensitivity maps using real *TESS* Science Processing Operations Centre (SPOC; Stassun et al. 2019) light curves from the Southern ecliptic hemisphere (Years 1 and 3). We combine these with occurrence rates to estimate a yield of planet discoveries.

We present the full details of the TIARA pipeline in Section 2 of this paper. In Section 3, we describe the application of the TIARA pipeline to the SPOC FFI (Full Frame Image) light curves from Yeasr 1 and 3 of the *TESS* mission. In Section 4, we present sensitivity maps and estimates of exoplanet yields from our simulation. In Section 5, we discuss interpretations of our results and some potential caveats and compare them to both actual *TESS* discoveries and other yield predictions. Finally, in Section 6, we summarize our work and discuss the potential for applying TIARA to additional *TESS* data sets as well as other transit surveys such as *PLATO* (*PLAnetary Transits and Oscillations of stars*; Rauer et al. 2014).

2 THE TIARA PIPELINE

In order to estimate the discovery yield of planets from transit surveys such as *TESS*, we need to simulate as many transiting exoplanet signals as possible in a realistic manner. To do this, we base our simulation on the actual stars that are monitored in the survey. We use the timestamps, measured noise properties, and dilution factors that are recorded for each star. We also use all available stellar properties such as radius ($R_\star$), temperature (T_{eff}), and mass ($M_\star$) – which are informed by *Gaia* data releases (Gaia Collaboration 2016, 2018, 2023).

In this section, we introduce the TIARA pipeline, which has been developed to calculate the sensitivity of a given transit survey to discovering transiting planets across a range of orbital periods and planetary radii. When combined with occurrence rates, this provides yield statistics for surveys that can be used to understand and assess the completeness of discoveries from a survey and plan future surveys.

2.1 Input of light curves

TIARA requires a catalogue of stars observed by a survey and their parameters. Using these target lists, we retrieve the relevant light curves for processing. We use the timestamps in the light curve to calculate a window function for each target star and to determine the number of in-transit datapoints when calculating the SNR for transit events. We also use measurements of noise values and dilution ratios for each light curve to calculate SNR for transit events. Using noise values calculated from real light curves allows for us to realistically account for a range of astrophysical and instrumental effects in the data. Similarly we use the dilution ratio to account for blending of sources which is a very common problem in wide field photometric transit surveys.

2.2 Simulating transiting planets

TIARA simulates transiting exoplanets by generating planet parameters and then calculates which timestamps are either occurring in the ingress, egress or fully in-transit portion of the transit event.

2.2.1 Generation of planetary parameters

Thanks largely to the *Kepler* mission (Borucki et al. 2010), we have a good understanding of the occurrence rates of exoplanets, particularly for those with orbital periods less than <100 d (Dressing & Charbonneau 2013, 2015; Fressin et al. 2013; Hsu et al. 2019; Kunimoto & Matthews 2020). For example, we know that super-Earth-sized exoplanets are far more common than gas giant planets in short-period orbits. We can take advantage of this understanding to optimize TIARA by simulating transiting planets in proportion to the occurrence rate of those planets. The occurrence rates we used are described in Section 3.7. Note that in including planets in the simulation proportionally to occurrence rates is *not* an attempt to simulate the underlying planetary population at this stage but instead is a measure to optimize the simulation. We prioritize injection of more numerous types of planets to avoid wasting simulation time on calculating a precise detection efficiency for rare types of planets for which the yield calculation will almost certainly be zero due to the small numbers in the underlying population. This means that the sensitivity maps we produce are still population agnostic, just with less precise values for rarer types of exoplanets.

We simulate a large number of planets per star (N_{Pl}) to obtain a more robust simulation. To choose the orbital period and radius of each of these we first select a period–radius bin using the occurrence rates as a weighted probability for a random draw. The exact period and radius of each planet in the sample was taken from a uniform distribution between the upper and lower limits of the chosen period and radius bins. We use the generated period and the mass of the star to estimate the semi-major axis using *Kepler*'s third law under the assumption that the mass of the planet is negligible compared to that of the star.

In order to ensure our simulated planets have a realistic eccentricity distribution, we randomly assign each planet an orbital eccentricity from a beta distribution following the prescription set out in Kipping (2013). We adopt the values of $\alpha = 1.03$ and $\beta = 13.6$ as proposed by Van Eylen & Albrecht (2015).

We randomly assign a periastron angle (ω) in radians, from a uniform distribution over the full π radian range.

For each planet generated, we calculated the geometric probability of transit (p_{tran}) following Winn (2014):

$$p_{\mathrm{tran}} = \left(\frac{R_\star + R_{\mathrm{p}}}{a}\right)\left(\frac{1 + e\sin\omega}{1 - e^2}\right). \tag{1}$$

For each simulated transiting planet, we randomly generate N_b different impact parameters (b) from a uniform distribution between the values of 0 and $1 + \frac{R_{\mathrm{p}}}{R_\star}$.

2.2.2 Simulation of transits

We calculate the total transit duration (T_{14}) including the ingress and egress between the first and fourth points of intersection between the planetary and stellar discs using the following equation from Winn (2014):

$$T_{14} = \frac{P}{\pi}\arcsin\left[\frac{R_\star}{a}\frac{\sqrt{\left(1 + \frac{R_{\mathrm{p}}}{R_\star}\right)^2 - b^2}}{\sin i}\right]\frac{\sqrt{1 - e^2}}{1 + e\sin\omega}, \tag{2}$$

where i is the inclination of the orbital plane and a is the semi-major axis of the orbit.

In addition, we also calculate the duration of transit between the second and third intersection (T_{23}) using the following equation from Winn ([2014](#)):

$$T_{23} = \frac{P}{\pi} \arcsin \left[\frac{R_\star}{a} \frac{\sqrt{\left(1 - \frac{R_p}{R_\star}\right)^2 - b^2}}{\sin i} \right] \frac{\sqrt{1 - e^2}}{1 + e \sin \omega}. \tag{3}$$

For grazing transits this does not give real solutions, and in such cases we simply set the value of $T_{23} = 0$.

To save computation time, we do not simulate signals with epochs that would result with zero in-transit data points. To accomplish this we convert the timestamps ingested by TIARA into orbital phase using a chosen reference time (TBJD=0 and BJD=2457000 for *TESS*) and use these phase arrays to determine which portions of the planets orbit are monitored by *TESS*. We then use these observed stretches of phase to generate random epochs in the form of an offset to the chosen reference time, expressed in orbital phase. These observed phase arrays also allow us to calculate the probability that any transit would randomly fall within an observed timespan of *TESS* (p_{obs}). We generate N_{ph} values of this phase offset for each inclination of each planet we simulate resulting in $N_b \times N_{ph}$ total transit signals per planet.

Using the values of T_{14} and T_{23} calculated from equations ([2](#)) and ([3](#)) and the epoch of each signal, we count the number of points in the timestamps of each light curve which are in ingress ($N_{ingress}$), egress (N_{egress}) or full transit (N_{full}). To obtain a more realistic value of the SNR we use a trapezoidal approximation for the shape of transit, and if the SNR calculation is likened to the effective area of the transit curve, then the ingress and the egress are triangular while the full transit is rectangular. Thus, the effective count of in-transit points for a trapezoidal transit is:

$$N_{\text{trans, eff}} = N_{full} + 0.5(N_{ingress} + N_{egress}). \tag{4}$$

It is worth noting that this trapezoidal model is a simplification of the actual shape of a transit and does not account for effects such as limb darkening (Espinoza & Jordán [2016](#); Agol, Luger & Foreman-Mackey [2020](#)). We believe this simplification is still robust enough to produce good yield estimates and discuss these effects further in Section [5.6](#)

2.3 Signal-to-noise calculation

A full injection and recovery test (e.g. Dressing & Charbonneau [2015](#); Hippke & Heller [2019](#); Bryant, Bayliss & Van Eylen [2023](#)) would require additional computation time to run a detection algorithm (e.g. BLS; Kovács, Zucker & Mazeh [2002](#); Collier Cameron et al. [2006](#)) on the data and to initialize a full transit model such as those produced by the BATMAN package (Kreidberg [2015](#)). We instead calculate detection based purely on the SNR for each signal based on the generated planet and light-curve properties.

The width of the transit is equal to the effective number of in-transit points from equation ([4](#)) multiplied by the time cadence of the light curve (ΔT). For non-grazing transits where ($0 \leq b < 1 - \frac{R_p}{R_\star}$) the depth of transit is simply:

$$\delta = \left(\frac{R_p}{R_\star}\right)^2. \tag{5}$$

For grazing transits ($1 - \frac{R_p}{R_\star} \leq b \leq 1 + \frac{R_p}{R_\star}$), we calculate the true anomaly at the time of mid-transit in accordance with Maxted ([2016](#)).

Table 1. Gamma function coefficients.

N_{tr}	$\alpha_{N_{tr}}$	$\beta_{N_{tr}}$	$c_{N_{tr}}$	Source
1	34.3932	0.254262	0.560547	This work
2	33.8908	0.259367	0.629820	This work
3	33.3884	0.264472	0.699093	Hsu et al. ([2019](#))
4	32.8860	0.269577	0.768366	Hsu et al. ([2019](#))
5	31.5196	0.282741	0.833673	Hsu et al. ([2019](#))
6	30.9919	0.286979	0.859865	Hsu et al. ([2019](#))
7–9	30.1906	0.294688	0.875042	Hsu et al. ([2019](#))
10–18	31.6342	0.279425	0.886144	Hsu et al. ([2019](#))
19–36	32.6448	0.268898	0.889724	Hsu et al. ([2019](#))
≥37	27.8185	0.32432	0.945075	Hsu et al. ([2019](#))

We then use equation (5.63) from Hilditch ([2001](#)) to calculate the corresponding projected orbital separation. We then calculate the depth of transit as the overlap in area between the planetary and stellar discs at this projected separation.

In either case, we then calculate SNR using the equation below:

$$SNR = \frac{\delta}{1 + C} \frac{\sqrt{N_{\text{trans, eff}} \Delta T}}{\sigma}, \tag{6}$$

where the contamination ratio (C) is the proportion of flux from background objects rather than the target itself, ΔT is the time cadence of the light curve, and σ is the light-curve noise on the time-scale of ΔT. This allows us to account for changes in cadence of observations such as the change from 30 to 10 min cadence between Years 1 and 3 of *TESS* FFIs.

2.4 Detection probability

To convert from SNR to a recovery rate, we need a function that encapsulates the likelihood that a given signal with a certain SNR will be detected as a transit candidate. Previous studies (Sullivan et al. [2015](#); Bouma et al. [2017](#); Barclay et al. [2018](#); Cooke et al. [2018](#); Huang et al. [2018](#); Villanueva et al. [2019](#)) have used an SNR threshold of SNR ≥ 7.3 to determine whether a planet is detectable. This approach is essentially a step function, where the probability of detecting a transit at SNR ≥ 7.3 is unity and the probability of detecting a transit at SNR < 7.3 is zero. Kunimoto et al. ([2022](#)) used an incomplete gamma function (γ) initially fitted to the *Kepler* pipeline by Christiansen ([2017](#)) and Hsu et al. ([2019](#)), to characterize the probability of a planet being both detected and passing vetting. The form of this function is:

$$p_\gamma(\text{det}) = c_{N_{tr}} \times \gamma \left(\alpha_{N_{tr}}, \frac{SNR}{\beta_{N_{tr}}} \right), \tag{7}$$

where $c_{N_{tr}}$ is the maximum probability of detection a transit signal with N_{tr} observed transits can reach and $\alpha_{N_{tr}}$, $\beta_{N_{tr}}$ are coefficients determined from the value of N_{tr} using Table [1](#).

For determining a detection probability, TIARA uses the *Kepler* gamma functions set out in Christiansen ([2017](#)) and as adopted by Hsu et al. ([2019](#)). For testing and comparison purposes, TIARA can also used a fixed detection threshold such as SNR ≥ 7.3.

In Hsu et al. ([2019](#)), there is no detection probability function defined for the case of only one or two transit events in the light curve. However calculating the yields for monotransits and duotransits is a key aspect of the TIARA pipeline. Therefore, we perform a linear extrapolation of the coefficients fitted by Hsu et al. ([2019](#)) to obtain values for $N_{tr} = 1$ and 2 resulting in Table [1](#). The incomplete gamma function is represented graphically for each set of coefficients in Fig. [2](#).
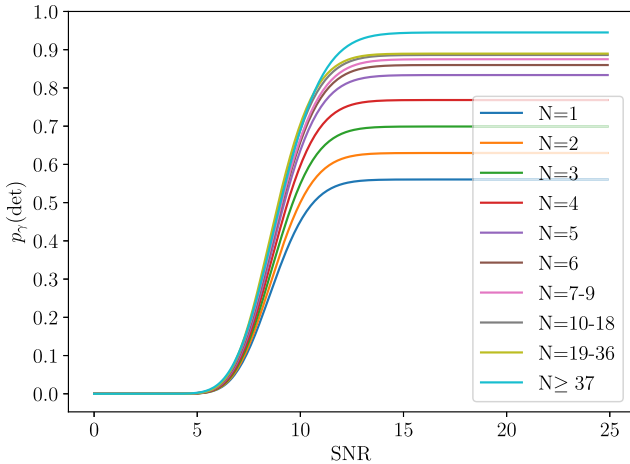
Figure 2. The set of incomplete gamma functions used as detection probability functions in the TIARA pipeline. Each function shows the probability a planet will be detected given the SNR of its transit signal in the light curve. The curves are each for a different number of individual transit events in the light curve (increasing vertically by one with each curve). The monotransits and duotransits are represented by the bottom (blue), $N=1$ and second from bottom (orange), $N=2$ functions, respectively.

Applying a gamma function based on the detection efficiency of *Kepler* to other surveys such as *TESS* comes with caveats as different detection pipelines will have different performance for the same SNR value. The effects of this on our yield predictions for *TESS* is discussed further in Section 5.7

2.5 Minimum detectable radius cut-off

Since we inject planets proportionally to their real occurrence rates, we will simulate many more smaller radius planets than larger planets due to their relative occurrence rates. However many of the smaller planets would produce transits with extremely low SNR, which may be far below the level of detectability in a given survey. Therefore to conserve computational resources and increase the efficiency of the simulation, we implement a radius cut-off to the occurrence rates based on the precision of the given survey. To do this, we estimate the minimum detectable radius from a single transit.

To calculate the minimum detectable radius, we assume a favourable set of transit parameters which consist of $e = 0$, $b = 0$, and T_{dur} set to a 'long' transit duration – defined to be the duration of a $P = 1000$ d transiting exoplanet of negligible radius around the given host star. Since SNR increases with transit duration, this long duration – beyond what we expect to realistically transit, was chosen so that small-radius planets which could be detected from a long enough transit were not removed from the simulation.

We choose an SNR threshold of 4 to determine the minimum detectable radius as this correlates with a very low probability of detection: $<10^{-5}$ (see Section 2.4). For planets with radii below the cut-off, we simply assign a probability of detection equal to 0.

3 *TESS* SIMULATIONS

3.1 *TESS* SPOC FFI light curves

In this study, we apply TIARA to the Years 1 and 3 FFI (Ricker et al. 2014) light curves from the *TESS* SPOC (Jenkins et al. 2016). The SPOC FFI light-curve sample is a high quality, homogeneous,

and readily availiable data set representing *TESS* targets which are most amenable to exoplanet detection and thus is appropriate for our purposes (Caldwell et al. 2020). Additionally, the *NGTS* monotransit working group uses the SPOC FFI light curves in their search for *TESS* monotransits (e.g. Gill et al. 2020) which allows for easy comparison of our results. We compiled the SPOC FFI target lists per *TESS* sector from MAST (Mikulski Archive for Space Telescopes) availiable at https://archive.stsci.edu/hlsp/tess-spoc into a single list containing the *TESS* Input Catalogue (TICv8; Stassun et al. 2019) numbers of all the SPOC FFI target stars and the *TESS* sectors they were observed in. We also removed all stars with radii $<0.1\mathrm{R}_\odot$ and $>4\mathrm{R}_\odot$ from the sample. This results in a sample of 1 323 228 stars across Years 1 and 3. For every star in this list, we obtained the relevant light curve FITS files via the MAST portal at https://archive.stsci.edu/.

3.2 Stellar parameters

We extracted the stellar radius ($\mathrm{R}_\star$), *TESS* magnitude (T_{mag}), and effective temperature (T_{eff}) directly from the FITS file headers: These stellar parameters are themselves sourced from the TICv8 (see Stassun et al. 2019).

To calculate a semi-major axis for our injected planets, we require a stellar mass ($\mathrm{M}_\star$). Due to a large number of targets lacking a value of the stellar mass in the light curve FITS file headers, we estimate the stellar mass using the following power law, which is approximated from the mass and radius of binary stars (Harmanec 1988):

$$\mathrm{M}_\star = \mathrm{R}_\star{}^{1.25}, \tag{8}$$

where $\mathrm{M}_\star$ and $\mathrm{R}_\star$ are both in solar units. The dependence of the semi-major axis on stellar mass is relatively weak and thus has a minor effect on planet detectability, therefore this power law is adequate for the main-sequence dwarf stars in the SPOC FFI sample. We assign a spectral type to each star based on T_{eff} using definitions from Pecaut & Mamajek (2013). Stars with T_{eff} hotter than the maximum cut-off for A type stars (10050 K) were marked as spectral type OB.

3.3 Window functions

In order to use the real window function for each star in the SPOC FFI list, we determine blocks of continuous *TESS* observations for each target using the timestamps from the FITS file TIME header for each *TESS* sector. We only consider good quality data where the data quality flag (QUALITY) = 0. We use the first and last timestamps of each Sector to define the block of continuous data for each Sector. To identify gaps within Sectors, we search for instances where the difference between two consecutive timestamps is greater than 0.5 d. Most of these gaps are the mid-Sector gaps, which occur during the perigee of the 13.7 d *TESS* orbit when data are downloaded to ground stations (Ricker et al. 2014). Other data gaps are caused by technical issues with the specific *TESS* camera, the entire *TESS* spacecraft, or the variety of reasons that give rise to non-zero data quality flags (e.g. stray light, cosmic rays, spacecraft momentum dumps, and pointing issues).

To illustrate these data gaps, we plot the light curve of a typical SPOC FFI target (TIC-261236954) in Fig. 3. TIC-261236954 is in the *TESS* CVZ, so can be used to illustrate gaps over the duration of Year 1 of the *TESS* mission. For this star the blocks of continuous photometry account for 79.3 per cent of the total Year 1 duration, while the gaps make up 20.78 per cent of that year.

In order to demonstrate the effect of these gaps in the *TESS* window functions, we calculate the fraction of orbital phase covered
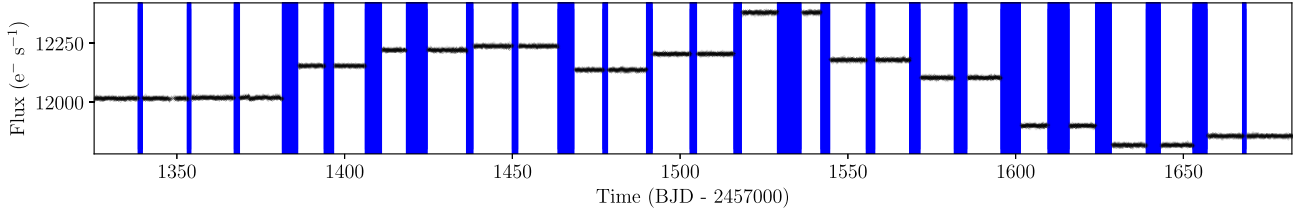
Figure 3. An example SPOC FFI light curve from a star (TIC-261236954) in the CVZ of *TESS* in Year 1 of the mission, illustrating gaps in the data. The vertical blue-shaded regions show data gaps longer than 0.5 d. In this example, we find that over the course of one year 79.3 per cent of time is photometrically monitored, while the gaps account for 20.7 per cent of the year.
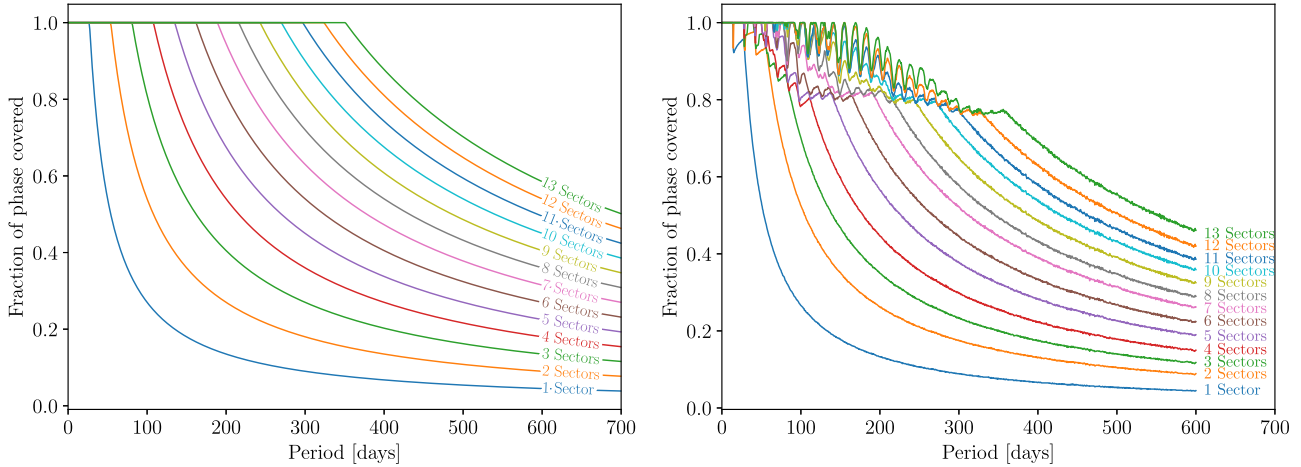

Figure 4. Completeness of phase coverage as a function of planetary orbital period. Left: idealized 27-d coverage (no gaps) for durations ranging from 1 to 13 consecutive sectors. Right: the real phase coverage function for an example SPOC FFI target (TIC-261236954) in the *TESS* CVZ.

by *TESS* observations as a function of the orbital period of a simulated planet for two scenarios: (1) an idealized 27-d window function, and (2) the window function of TIC-261236954 (the light curve for which is set out in Fig. 3. This allows us to compare the effect of gaps for up to 13 consecutive Sectors. The results are set out in Fig. 4, and show the significant difference between the idealized 27 d Sectors and the real TIC-261236954 light-curve window function. This highlights the need to account for the gaps in the *TESS* data for each star as we do in the TIARA pipeline. We note that different pipelines may use different data quality flags, which may slightly alter the position and/or duration of some of the data gaps.

3.4 Signal to noise

To calculate the SNR (equation 6) for each simulated transiting planet, we take the noise of the light curve (σ) to be the Combined Differential Photometric Precision (CDPP; Christiansen et al. 2012) 2 h noise as produced by the SPOC FFI pipeline and recorded in the FITS headers as CDPP_20. This provides us with a readily available pre-calculated noise metric, which saves computation time. Similarly we take the source-to-background brightness ratio ($C + 1$) from the SPOC FFI pipeline recorded in the FITS headers as CROWDSAP. The time cadence (ΔT) has changed over the course of the *TESS* mission. For Year 1 the time cadence was 30 min, while for Year 3 the time cadence was 10 min.

3.5 Probability of detection

We assume that the detection and vetting of transiting exoplanet signals in *TESS* is similar to that of the *Kepler* mission, and we therefore use the the modified version of the *Kepler* gamma function (Section 2.4) to define our probability of detection for each simulated transiting planet. For comparative purposes, we also record detections via two threshold SNR criteria: at SNR ≥ 7.3 (to match some previous yield studies) and SNR ≥ 20 (to match monotransit searches that typically require such a high SNR for robust detections).

3.6 Creating sensitivity maps

For each transit signal that we generate, we convert the SNR into detection probability as described in Section 3.5. Each of these probabilities is then multiplied by the probability of observation for each signal calculated from its window function (see Section 3.3) to give a probability of observation and detection. These values are again multiplied by the geometric probability of transit for each signal to give a probability of transit, observation and detection by *TESS* for each signal. We take the binned averages for all signals using the same period and radius bins as Kunimoto & Matthews (2020).

We treat each of our detection probabilities as a Poisson statistic such that the error in each is equal to its value divided by the square root of the total count of signals in that bin.

3.7 Occurrence rates

In order to convert our sensitivity maps to yield estimates for the Years 1 and 3 *TESS* SPOC FFI sample, we need to know the occurrence rates for the underlying population of planets orbiting each type of star in the sample. For F, G, and K dwarf stars we use the occurrence rates calculated in Kunimoto & Matthews (2020). For A type stars, we do not have robust occurrence rates, so we use the same grid as for F type stars.

Kunimoto & Matthews (2020) did not calculate occurrence rates for M dwarfs, so for consistency and ease of comparison between our results we rebin the M dwarf occurrence rate grid from Dressing & Charbonneau (2015) to use the same bins as the grids used in Kunimoto & Matthews (2020). To do this we use a bivariate spline approximation over a rectangular mesh using the RECTBIVARIATE-SPLINE interpolator from the PYTHON module; SCIPY.INTERPOLATE (Virtanen et al. 2020). We take the mid-points of each period and radius bin from the Dressing & Charbonneau (2015) grid and use these for the coordinates of each grid value. We then used the median value, lower bound, and upper bound of each grid cell with these coordinates to create three separate interpolators for each value. We then feed the midpoints of all the Kunimoto & Matthews (2020) bins with $R_p \leq 4R_\oplus$ and an orbital period $\leq$200 d into these to obtain the values for the new grid. For the 200–400 d period bin, we assume the values were identical to the 100–200 d bin. For all bins above $4R_\oplus$, we use the values for K dwarf stars but reduced by a factor of 0.5 to account for the generally lower occurrence rates of giant planets around M dwarfs (Sabotta et al. 2021; Bryant et al. 2023; Gan et al. 2023).

To account for the fact that some bins in the grid from Dressing & Charbonneau (2015) are unconstrained and contain only an upper bound on the occurrence rate we manually set the equivalent grid cells in our new grid to be unconstrained as well. For all such grid cells, we set the median and lower bound values to zero and the upper bound value to the interpolated median value added to the interpolated upper bound value. We consider the new grid cells between 0.78–1.56 d and 2–4 $R_\oplus$, 6.25–25 d and 1–1.41 $R_\oplus$, 50–200 d and 0.5–1$R_\oplus$ and 2.83–4$R_\oplus$, to be equivalent to the old grid cells between 0.5–1.7 d and 2–4 $R_\oplus$, 5.5–18.2 d and 1.0–1.5 $R_\oplus$, 60.3–200 d and 0.5–1 $R_\oplus$ and 3.5–4 $R_\oplus$, respectively for the purposes of considering them unconstrained. Furthermore we also consider all the grid cells between 200–400 d and $<4R_\oplus$ to be unconstrained as these are extrapolated and not interpolated from the measured *Kepler* rates by Dressing & Charbonneau (2015) and such planets are shown to be very rarely detected by *TESS* if at all (NASA Exoplanet Archive; Akeson et al. 2013).

Our resulting M-dwarf occurrence rate grid is set out in Fig. 5.

The Dressing & Charbonneau (2015) occurrence rates were calculated prior to *Gaia*, and therefore the stellar parameters of candidates are not as robust as post-*Gaia* studies such as Hsu et al. (2019) and Kunimoto & Matthews (2020). Recently, Bergsten et al. (2023) have updated the Dressing & Charbonneau (2015) occurrence rates for small radius planets ($R_p < 2\,R_\oplus$). These small radii planets are unlikely to be detectable in the *TESS* data, so this update will not significantly impact the results we present in this paper. However, we plan to include these updated occurrence rates in future TIARA simulations.

3.7.1 Use as input priority metrics

As set out in Section 2.2.1, we also use occurrence rate grids as a weighted distribution to select periods and radii for planets we
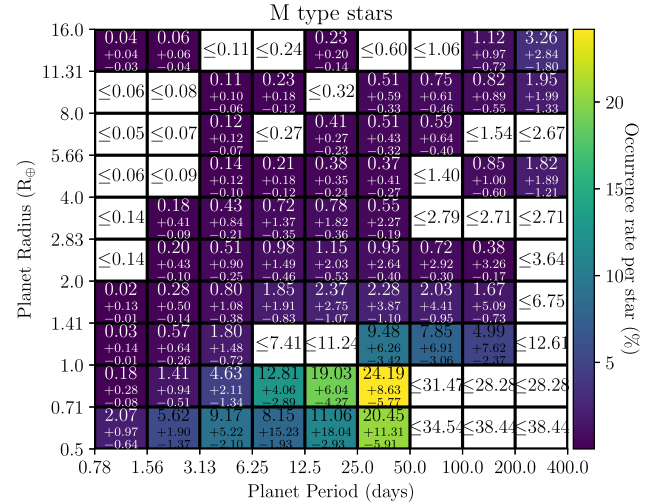
Figure 5. Percentage occurrence rates of planets around M dwarfs. Values for $R < 4\,R_\oplus$ taken from Dressing & Charbonneau (2015), rebinned to our standardized grid. Values for $R > 4\,R_\oplus$ from the a scaled K dwarf occurrence rate from Kunimoto & Matthews (2020).

M type stars

Planet Radius ($R_\oplus$) \ Planet Period (days)	0.78–1.56	1.56–3.13	3.13–6.25	6.25–12.5	12.5–25.0	25.0–50.0	50.0–100.0	100.0–200.0	200.0–400.0
16.0–11.31	0.04 +0.04 −0.03	0.06 +0.06 −0.04	≤0.11	≤0.24	0.23 +0.20 −0.14	≤0.60	≤1.06	1.12 +0.97 −0.72	3.26 +2.84 −1.80
11.31–8.0	≤0.06	≤0.08	0.11 +0.10 −0.06	0.23 +0.18 −0.12	≤0.32	0.51 +0.59 −0.33	0.75 +0.61 −0.46	0.82 +0.89 −0.55	1.95 +1.99 −1.33
8.0–5.66	≤0.05	≤0.07	0.12 +0.12 −0.07	≤0.27	0.41 +0.27 −0.23	0.51 +0.43 −0.32	0.59 +0.64 −0.40	≤1.54	≤2.67
5.66–4.0	≤0.06	≤0.09	0.14 +0.12 −0.10	0.21 +0.18 −0.12	0.38 +0.35 −0.24	0.37 +0.41 −0.27	≤1.40	0.85 +1.00 −0.60	1.82 +1.89 −1.21
4.0–2.83	≤0.14	0.18 +0.41 −0.09	0.43 +0.84 −0.21	0.72 +1.37 −0.35	0.78 +1.82 −0.36	0.55 +2.27 −0.19	≤2.79	≤2.71	≤2.71
2.83–2.0	≤0.14	0.20 +0.43 −0.10	0.51 +0.90 −0.25	0.98 +1.49 −0.46	1.15 +2.03 −0.53	0.95 +2.64 −0.40	0.72 +2.92 −0.30	0.38 +3.26 −0.17	≤3.64
2.0–1.41	0.02 +0.13 −0.01	0.28 +0.50 −0.14	0.80 +1.08 −0.38	1.85 +1.91 −0.83	2.37 +2.75 −1.07	2.28 +3.87 −1.10	2.03 +4.41 −0.95	1.67 +5.09 −0.73	≤6.75
1.41–1.0	0.03 +0.04 −0.01	0.57 +0.64 −0.26	1.80 +1.48 −0.72	≤7.41	≤11.24	9.48 +6.26 −3.63	7.85 +6.91 −3.06	4.99 +7.62 −2.37	≤12.61
1.0–0.71	0.18 +0.28 −0.08	1.41 +0.94 −0.51	4.63 +2.11 −1.34	12.81 +4.06 −2.80	19.03 +6.04 −4.27	24.19 +8.63 −5.77	≤31.47	≤28.28	≤28.28
0.71–0.5	2.07 +0.97 −0.64	5.62 +1.90 −1.37	9.17 +5.22 −2.10	8.15 +15.23 −1.93	11.06 +18.04 −2.93	20.45 +11.31 −5.91	≤34.54	≤38.44	≤38.44

Occurrence rate per star (%)

inject into the simulation. This requires us to set a median value for unconstrained grid cells that possess only an upper bound. For the A, F, G, and K dwarf grids, we perform a linear extrapolation of each grid row and column and then take the mean of these as the input grid. For the M dwarf grid, we simply take the upper bound of unconstrained grid cells as the median value.

3.8 Yield estimates

To calculate our final yield estimates we multiply the occurrence rates by the detection efficiencies for each spectral type, and then multiply those rates and their uncertainties by the number of each type of star in the Years 1 and 3 SPOC FFI sample. This gives us a grid of expected yields for each period–radius bin with uncertainties combined from those of the detection sensitivities and occurrence rates. The error in occurrence rate is considerably larger and so dominates the overall uncertainty in predicted yield.

4 RESULTS

4.1 *TESS* sensitivity

The TIARA pipeline creates binned sensitivity maps on the same grid as the occurrence rates from Kunimoto & Matthews (2020). These show the probability that a transiting exoplanet of a given radius and orbital period is observed and detected by *TESS* in the Years 1 and 3 SPOC FFI light curves. We compute separate sensitivity maps for each of A,F,G,K, and M dwarfs, and these are set out in Appendix A Fig. A1. We also plot the average sensitivity for AFGKM dwarfs in the SPOC FFI sample in Fig. 6. The uncertainties in sensitivity are very small, this is largely on account of the large numbers of signals we inject in the simulation, which allows for such precise calculation.

Naturally, there is a trend of higher sensitivity towards larger radii planets as these planets produce deeper transits and thus a higher SNR signal. We find that *TESS* should detect over 80 per cent of very short period ($P < 6.25$ d), transiting giant planets ($R > 8\,R_\oplus$). This probability drops below 50 per cent for small transiting planets ($R < 4\,R_\oplus$), and is below 1 per cent for Earth-radii transiting planets.
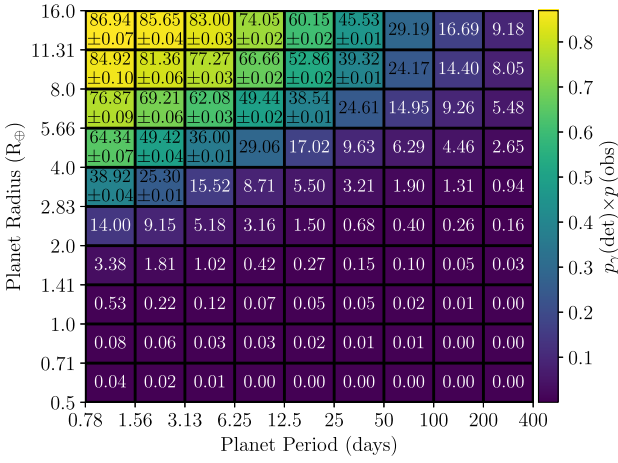
Figure 6. Sensitivity map showing the probability of a transiting planet in each period/radius bin being observed and detected around an AFGKM dwarf star in the *TESS* Years 1 and 3 SPOC FFI light curves. The percentage sensitivity values are shown in each grid cell. Where no uncertainties are given the uncertainty is 0 per cent to two decimal places.

Figure 7. Predicted exoplanet yield from Year 1 and 3 SPOC FFI light curves of AFGKM type stars. Note that cells where the median value is 1 have been displayed as ≤1 to account for the inherent uncertainty in a predicted yield of 1.

Additionally, we are more sensitive to shorter period planets due to the greater number of observed transits in any given monitoring duration. This both produces a higher SNR value when these transits are summed and allows for greater confidence in the detection as accounted for by the gamma function we use to calculate probability of detection (see Section 3.5). For giant planets ($R > 8\,R_\oplus$), we move from approximately 80 per cent completeness for short periods ($P < 6.25$ d) down to less than 10 per cent completeness for periods between 200 and 400 d.

As the *TESS* mission continues, these sensitivity maps will evolve as a function of the window function for each star, and the sensitivity will improve over the entire grid. TIARA will be able to re-calculate these sensitivity maps using the timestamps from *TESS* light curves as the extended *TESS* mission continues to gather data. For the Southern ecliptic hemisphere, this will be the update provided by the Year 5 light curves (Sectors 61–69). It is also possible to simulate timestamps for future sectors based on our knowledge of previous sectors with some assumptions needed for distribution of the future data gaps and FFI cadence.

4.2 Predicted yield

We present the TIARA predicted yield of transiting exoplanet discoveries from *TESS* Years 1 and 3 SPOC FFI light curves in Fig. 7. This grid is the summation of all spectral types, however we also present the yields broken down by spectral type in Appendix B (Fig. B1).

Overall we predict a yield of 2271^{+241}_{-138} exoplanets detected around AFGKM dwarf host stars. We set out the yield distributions of orbital period, planet radius, and host spectral type in Fig. 8. We find the discoveries should peak at orbital periods between 3.13 and 6.25 d. However there are a significant number of longer period planets in our predicted yield, with 403^{+64}_{-38} planets with orbital periods greater than 25 d and 113^{+23}_{-17} will have orbital periods greater than 100 d. Interestingly the distribution of planet radii is quite flat, with the exception of giant planets ($R > 11.31 R_\oplus$), which are twice as numerous as other radius bins. Most discoveries are predicted to be around G dwarf stars, although K dwarfs provide the most number of discoveries per star monitored.
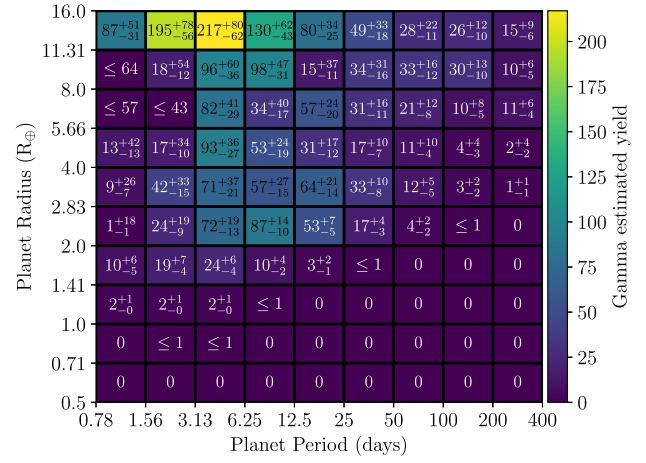
To compare our predicted yield to the actual discoveries, we cross-match the TOI (*TESS* objects of interest) catalogue as of 2023 June 15 with the SPOC FFI target lists for Years 1 and 3 to find transiting exoplanet discoveries from our sample. The distributions of these TOIs and our predicted yields are shown in Fig. 8.

4.3 Monotransits

We predict that 215^{+37}_{-23} of the transiting planet discoveries will only have one transit event in the *TESS* Year 1 or Year 3 data – that is, are 'monotransits'. This makes up a relatively small fraction (9 per cent) of the total predicted yield, but is a significant fraction of the long-period detections. 202^{+36}_{-22} (50 per cent) of the planets with $P > 25$ d are monotransits, while 86^{+20}_{-14} (76 per cent) of the planets with $P > 100$ d are monotransits. Fig. 9 shows the the distributions of orbital period and planetary radius for the predicted monotransit yield. As expected there are very few monotransits with orbital periods less than the sector length of *TESS* (27 d). However beyond that the distribution of orbital period is remarkably flat out to our final bin of 400 d. The distribution of planetary radii for the monotransits are much more heavily skewed towards larger radii planets than typical multitransit detections. 73 per cent of all detections are for planets with $R_{\rm p} > 4\,R_\oplus$, while this fraction is 94 per cent of just the monotransit detections.

In addition to the monotransit yield for Years 1 and 3 together, we also estimated the yield for Year 1 alone in order to investigate the effect of re-observing the field on the monotransit yield. The results are shown in Fig. 10. We find that the number of monotransits in Year 1 alone is 227^{+36}_{-20}, compared to the Years 1 and 3 combined yield of to 215^{+37}_{-23}. Assuming that all of the Year 1 monotransits that have an additional Year 3 transit observed become duotransits (see Section 4.4), then this leaves 114^{+42}_{-24} detected monotransits observed in Year 1 and not Year 3 and 101^{+55}_{-33} observed in Year 3 and not Year 1. The distribution of orbital periods changes to favour longer periods with 40 per cent of Years 1 and 3 monotransits having $P > 100$ d compared to 26 per cent of Year 1 only monotransits. The distribution of monotransit detections in period also becomes significantly flatter at longer periods when Year 3 is added to Year 1.
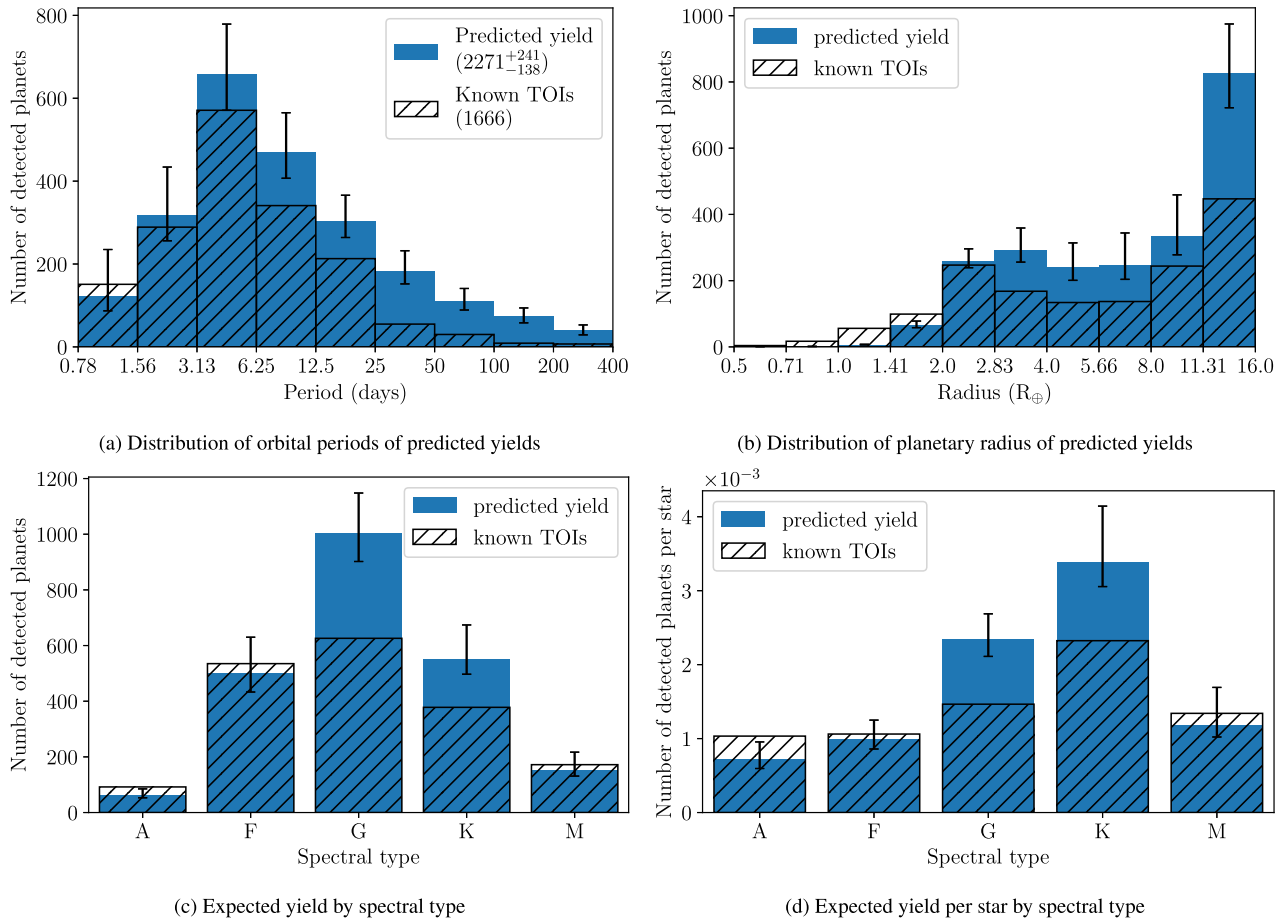
(a) Distribution of orbital periods of predicted yields

(b) Distribution of planetary radius of predicted yields

(c) Expected yield by spectral type

(d) Expected yield per star by spectral type

Figure 8. Predicted TIARA transiting exoplanet yields from the *TESS* Years 1 and 3 SPOC FFI light curves (solid blue bars). Also displayed are actual *TESS* discoveries (transparent black outlined and diagonally hatched bars) calculated using TOI catalogue downloaded from the NASA exoplanet archive (Akeson et al. 2013) on 2023 June 15 (excluding flagged false positives) and matched to TIC IDs of southern ecliptic SPOC FFI sample.

(a) Period distribution of predicted monotransit detections

(b) Radius distribution of predicted monotransit detections
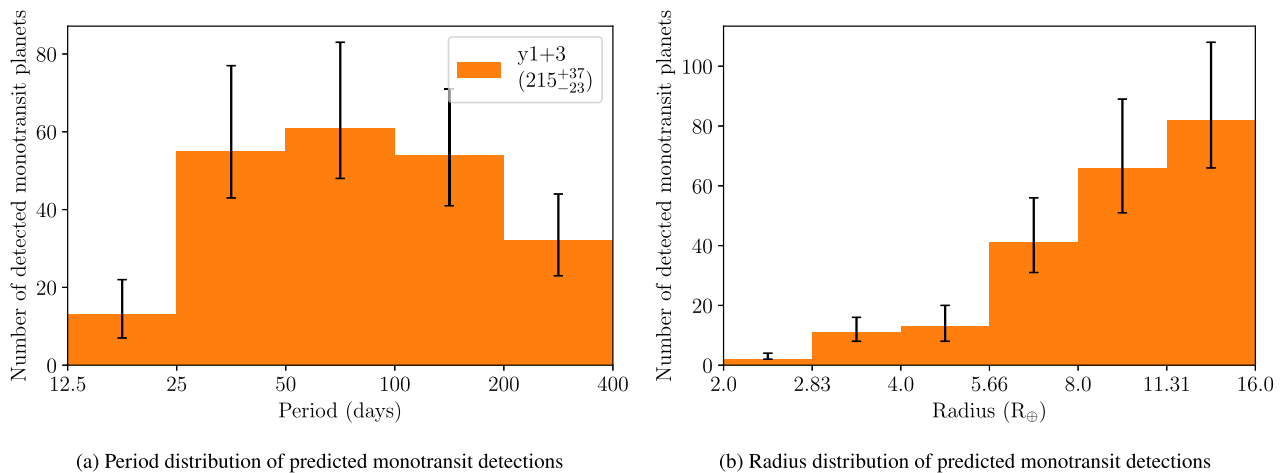
Figure 9. Predicted yields of monotransits, shown as binned distributions in (a) orbital period and (b) radius.

4.4 Duotransits

As *TESS* reobserved the Southern ecliptic hemisphere in Year 3 of the mission, many Year 1 monotransit signals will have an additional transit observed in Year 3, and become 'biennial duotransits'. We define these duotransits as 'biennial' to distinguish them from other duotransits in which the two transit events happen in the same year of *TESS* data.. We predict a total of 170^{+29}_{-18} duotransits in total with 113^{+22}_{-13} of these being biennial duotransits.

The distribution of biennial duotransits is shown in Fig. 11. Compared to monotransit detections (see Section 4.3), we find that
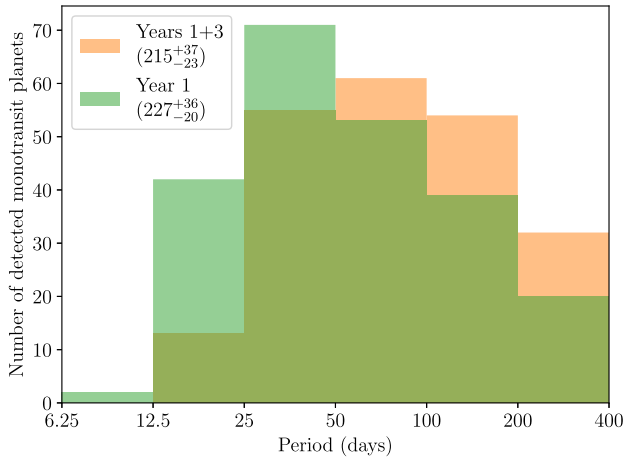
Figure 10. Comparison of the distribution in period of the yields of monotransits from Year 1 alone (green/foreground) compared to Years 1 and 3 combined (orange/background).

the sample of planets detected from biennial duotransits show a flatter distribution in radius, with 21 per cent of biennial duotransit detections coming from planets below $4\,R_\oplus$ compared to 6 per cent of monotransits, although radii $>11.31\,R_\oplus$ are still the largest bin of detections. We find the period of expected biennial duotransits peaks between 25 and 50 d and falls off more rapidly than monotransits for longer periods, with 6 per cent of biennial duotransits coming from periods >100 d compared to 40 per cent of monotransits.

4.5 Breakdown by spectral type

As shown in Fig. 8(c), we find G dwarfs should be host to the most detections (1005^{+143}_{-103}), followed by K (551^{+123}_{-54}) and F (500^{+130}_{-67}) dwarfs in quick succession with a reasonable number from M dwarfs (151^{+66}_{-20}) and a very small number from A dwarfs (64^{+21}_{-11}). This distribution is largely due to the numbers of each spectral type represented in the SPOC FFI sample with G types being the most numerous and thus host to the most detected planets.

Fig. 8(d) shows the yield from each spectral type divided by the number of stars of that spectral type in the SPOC sample. From this it becomes apparent that K dwarfs are the most numerous hosts of detections per star with a rate of $(3.4^{+0.8}_{-0.3}) \times 10^{-3}$ transiting planets per star observed. G dwarfs are the next most efficient sources of detections with $(2.4^{+0.3}_{-0.2}) \times 10^{-3}$ predicted per star, followed by M with $(1.2^{+0.5}_{-0.2}) \times 10^{-3}$, F with $(0.99^{+0.26}_{-0.13}) \times 10^{-3}$ and A with $(0.72^{+0.24}_{0.12}) \times 10^{-3}$.

K dwarfs sit at the best crossover between occurrence rates and *TESS*' detection efficiency, and thus have the highest rate of detections per star. Despite M dwarfs having higher planetary occurrence rates than AFGK stars (Dressing & Charbonneau 2015) and their small size causing deeper transits due to a higher planet–star radius ratio, they display a relatively low rate of detections per star. M dwarfs host many small radius planets compared with AFGK dwarfs, but fewer giant planets. These small planets produce low SNR signals that result in low detection probabilities for M dwarf host stars. This results in fewer detections per star for M dwarfs.

Fig. 12 shows the proportion of different period ranges in the predicted yield by spectral type. We find a reasonably flat trend in the distribution of long-period discoveries for each spectral type with a possible minor trend towards shorter period discoveries being favoured at later spectral types, although increasingly small numbers create uncertainty in such a trend.

4.6 Comparison on detection probability functions

As well as the gamma function described in Section 2.4, we also calculate yields using simple SNR threshholds of 7.3 and 20. Fig. 13 shows a comparison of the results from these three approaches.

The predicted total yield using an SNR ≥ 20 threshold of 1555^{+216}_{-126} shows a strong agreement with the total number of TOIs from the Years 1 and 3 SPOC FFI discoveries (1666). However Fig. 13 demonstrates that the predicted distribution in periods and radii from this criterion does not match the proportions of the TOI sample as well as other methods. We see a significant underprediction of planet yields for radii below $5.66\,R_\oplus$ which increases in disagreement for decreasing radii from this method as shown in Fig. 13(b). We also find that the yields for short-period planets ($P < 25$ d) are underpredicted by this method, with the largest deficit being between 3.13 and 6.25 d.

Using a smaller SNR threshold of 7.3 as many yield studies have done previously (e.g. Sullivan et al. 2015; Bouma et al. 2017; Barclay et al. 2018; Cooke et al. 2018, 2019; Villanueva et al. 2019), we find a significantly greater yield prediction than either the threshold of SNR ≥ 20 or the gamma function. The predicted yield of planets with SNR ≥ 7.3 (3334^{+309}_{-177}) is more than double the size of the TOI discoveries and the yield predicted by SNR ≥ 20 and around 1.5 times greater than that predicted by the gamma function. A large fraction of this additional predicted yield comes from small planets and longer period planets as shown in Fig. 13.

5 DISCUSSION

5.1 Comparison to actual *TESS* detections

Comparison to the population of *TESS* transiting planet discoveries via the TOI catalogue is a relatively straightforward and robust check for the TIARA yield results. We cross-match the TIC IDs of the TOI catalogue with stars we simulated from the SPOC FFI sample to compare against our predicted yields as shown in Fig. 8.

While we use the SPOC FFI light curves as a homogeneous sample it must be noted that the TOI sample is not generated homogeneously. While we limit the TOI catalogue to just those which have SPOC FFI light curves which we include in our simulation, many of these will still have been discovered in light curves produced by other pipelines such as the SPOC 2 min postage stamp or Quick look light curves (QLP; Huang et al. 2020). These light curves may have different duty cycles, noise levels, and systematics to the SPOC FFI sample we use. Different quality flags in these pipelines may also affect the location and duration of data gaps between data products. Additionally the automated TOI search carried out is different between pipelines, which means TOIs from different pipelines are affected by different biases. It is for this reason that we stress that our comparison is not specifically an attempt to assess the completeness of the SPOC FFI pipeline TOI search.

Our total predicted yield of 2271^{+241}_{-138} is $\sim 4.4\sigma$ greater than the total number of TOIs (1666) as of 2023 June 15. However, for orbital periods less than 6.25 d, the TIARA predictions agree with the discoveries to within uncertainties. For periods between 6.25 and 25 d, the TIARA predictions are not more than 2σ above the discoveries. However for planets with periods greater than 25 d the deficit between TIARA predictions and TOI discoveries becomes increasingly significant as shown in Fig. 14.
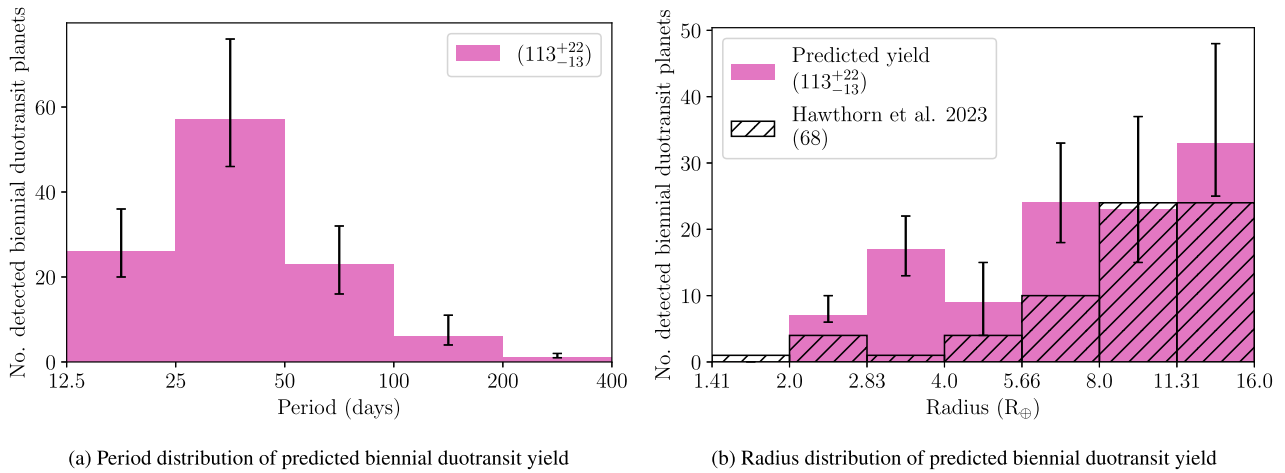
(a) Period distribution of predicted biennial duotransit yield

(b) Radius distribution of predicted biennial duotransit yield

Figure 11. Predicted yields of biennial duotransit planets detected from one transit in Year 1 and another in Year 3. Shown in distributions of (a) period and (b) radius. Plot (b) also shows a comparison with the radii of biennial duotransits from Hawthorn et al. (2023) excluding candidates over $16\,R_\oplus$ which we do not simulate.
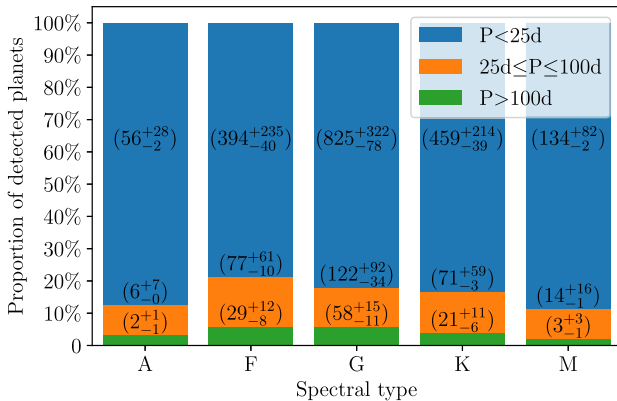

Figure 12. Comparison of the proportions of predicted long-period planet yield by spectral type. Planets with periods less than 25 d are shown in blue (top), periods between 25 and 100 d are shown in orange (middle), and periods longer than 100 days are shown in green (bottom). The predicted yield numbers for each spectral type and period range are printed on the plot, along with the associated uncertainties.

The SPOC Transiting Planet Search (TPS, Jenkins et al. 2016; Guerrero et al. 2021) relies on phase folding data to search for periodic signals (Guerrero et al. 2021). This becomes increasingly difficult for longer periods as such planets may have transits in different *TESS* sectors or only one transit which is impossible to phase fold. This suggests that the difference between our predicted yield and the TOI sample may be due to *TESS* discoveries being currently incomplete for longer period planets. Since the majority of candidates are given TOI status by the TPS (Guerrero et al. 2021), many monotransit and biennial duotransit events in the SPOC FFI light curves may have yet to be detected.

It is difficult to uniformly simulate the planet detection process that makes up the TOI catalogue, as the TOI catalogue is not built up from a single uniform search of the SPOC FFI light curves. Instead the SPOC TPS only runs on selected postage stamp light curves (around 20 000 per sector), while the rest of the SPOC FFI targets are searched by Quick Look Pipeline (QLP; Huang et al. 2020). However, the QLP operates at a hard magnitude cut-off of $T = 13.5$, and some

of the SPOC FFI targets are fainter than this cut-off. Therefore some of the light curves in the SPOC FFI sample have not been searched in a systematic manner. Additionally, third party groups will have their own methods of searching light curves for candidates which can lead to additional TOIs being created via the Community TOI process (CTOI; Guerrero et al. 2021). These subtleties could contribute to a small discrepancy between our predictions and the actual TOI catalogue, although significant differences are likely still due to incompleteness as described previously.

We can gain an indication of this by comparing our predicted yield with and without monotransits to the TOI sample. When we remove monotransits from our predicted yield we find 2056^{+245}_{-140} detected exoplanets and excluding biennial duotransits we further reduce this to 1943^{+246}_{-141}. This brings our yield into closer alignment with the TOI detections (taken from NASA exoplanet archive, Akeson et al. 2013) from 4.4σ to 2.8σ and 2.0σ, respectively.

This could also explain the seeming overabundance of giant planets as seen in Fig. 8(b) as long-period monotransit and duotransit detections are particularly biased towards larger radii (see Figs 9b and 11b), and hence the undiscovered long-period planets make up the majority of the undiscovered giant planets as well. Additionally it could explain the overestimation of planets detected around G and K dwarfs shown in Figs 8(c) and (d). As these stars make up the largest numbers of stars in the SPOC FFI sample and have the highest detection rate per star, it it likely that most of the long-period and other planets not yet found would be around these.

5.2 Comparison to biennial duotransit search

We are able to compare our predicted yield of biennial duotransit detections with a real search of the Years 1 and 3 SPOC FFI light curves for biennial duotransits set out in Hawthorn et al. (2023). Fig. 11(b) shows the distribution of the TIARA predicted yields and the sample from Hawthorn et al. (2023) in radius. The periods of the majority of candidates in Hawthorn et al. (2023) are currently unknown and so cannot be compared directly to our prediction. Our predicted yield of biennial duotransits is 113^{+22}_{-13}, which is 3.5σ greater than the 68 candidates in the real sample. The numbers are in close agreement for radii between 8.0 and $11.31\,R_\oplus$ and near agreement for 11.31 to $16\,R_\oplus$. However for smaller radii planets
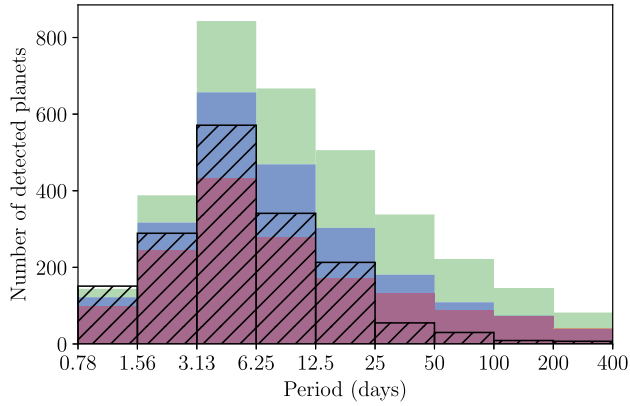
(a) Period distribution of predicted yields for three detection criteria
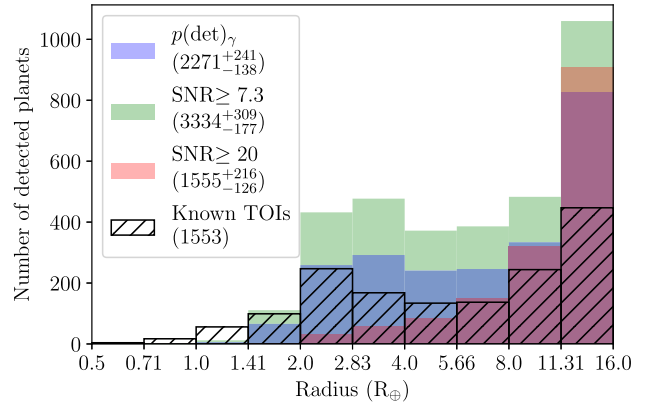
(b) Radius distribution of predicted yields for three detection criteria

Figure 13. Comparison of the yields predicted using three different detection criteria, a gamma cumulative distribution (blue), and SNR thresholds of 7.3 (green) and 20 (red). Distributions are shown in (a) period and (b) radius.
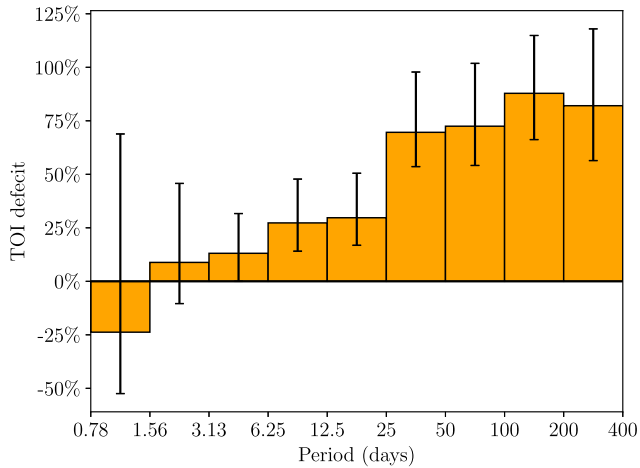

Figure 14. Percentage deficit between the discovered TOIs and our predicted yield for the *TESS* SPOC FFI light curves from Years 1 and 3.

$(R < 4\,\mathrm{R}_\oplus)$, TIARA predicts many more biennial duotransits than than are detected in Hawthorn et al. (2023), especially between 2.83 and $4\,\mathrm{R}_\oplus$. This is to be expected as Hawthorn et al. (2023) only consider high SNR biennial duotransits, which will be produced by larger planets. We note that Hawthorn et al. (2023) also have a significant number of candidates with radii larger than $16\,\mathrm{R}_\oplus$, however we do not consider such large radius objects in our TIARA simulation.

We also note the strong agreement between the predicted number of biennial duotransits with SNR ≥ 20 of 86^{+25}_{-13} and the discovery of 68 biennial duotransits from Hawthorn et al. (2023). The effect of using different probability of detection functions is discussed further in Section 5.7.

5.3 Comparison to previously predicted yield

In addition to comparing our results to the TOI catalogue (see Section 5.1) we can also check the validity of our results by comparing them to previous attempts at predicting yield. This is especially useful as our methods include monotransits, which are not included in studies such as Kunimoto et al. (2022).

Kunimoto et al. (2022) use a considerably larger population of stars. We have simulated the yield from the $\sim$1.3 million stars in the Years 1 and 3 SPOC FFI sample. Kunimoto et al. (2022) use 4 million stars from the *TESS* Candidate Target List (CTL; Stassun et al. 2019). Therefore, we normalize each set of results by the number of stars in each sample and compare in terms of number of planets predicted per star (similarly to in Fig. 8d) for ease of comparison. However, it should be noted that the selection criteria for each stellar sample, especially for SPOC stars (Caldwell et al. 2020), introduces biases in the average detectability for each stars, so this is somewhat of a crude comparison.

Kunimoto et al. (2022) predict a total of 2532 ± 189 exoplanets found around $4\,066\,063$ stars in Year 1 and 1748 ± 103 around $4\,021\,948$ stars in Year 3. This gives a total of $(1.06 \pm 0.05) \times 10^{-3}$ detections per star. This is $6.5\,\sigma$ below our estimate of $(1.55^{+0.18}_{-0.11}) \times 10^{-3}$ per star excluding monotransits. It is to be expected that our yield prediction will be greater than Kunimoto et al. (2022) since we use the SPOC FFI sample, which has been explicitly created to target stars that are most likely to have detectable transits with *TESS* (Caldwell et al. 2020).

5.4 Eccentricity distribution

As in Cooke et al. (2018, 2019), we use a beta distribution to assign eccentricity to planets we inject into our simulation and use values for α and β taken from Van Eylen & Albrecht (2015). However, this study was focused on super-Earths and Mini-Neptunes from *Kepler* and not longer-period giant planets which are the focus of this paper. Warm-Jupiters have been found to often show much higher orbital eccentricities than smaller and/or closer-in planets (Dong et al. 2021) and therefore we are likely underestimating the eccentricity of the warm-Jupiter population in our simulation. However eccentric long-period planets are more likely to transit at periastron when closer to their host stars and hence this means we are likely *underestimating* the detection sensitivity of *TESS* towards such planets.

5.5 Occurrence rates

The TIARA yield predictions rely on the occurrence rates from Kunimoto & Matthews (2020) for AFGK stars and a modified occurrence rate from Dressing & Charbonneau (2015) for M dwarfs.

The occurrence rates we use from Kunimoto & Matthews (2020) do not include any planets larger than $16\,R_\oplus$ although larger planets are known to exist and are likely to be detectable by *TESS* even if the occurrence rates from *Kepler* are known to be low (Fressin et al. 2013; Hsu et al. 2019; Kunimoto & Matthews 2020). Future yield estimate studies could benefit from studies into the occurrence rate of planets larger than $16\,R_\oplus$ which could be carried out on samples of planets from *TESS*.

Due to the lack of occurrence rate studies on A and earlier spectral-type stars, we assume the occurrence rates of planets around A and earlier type stars are equal to that of F type stars (see Section 3.7). In reality these may be different as the higher mass and temperature of A type stars are expected to have significant effects on planet formation and thus the occurrence rate (Johnson et al. 2010). Future studies could benefit from *TESS* derived occurrence rates of A type stars (e.g. Zhou et al. 2019; Johnson 2023).

For M dwarfs we rebin the values found by Dressing & Charbonneau (2015) onto the same grid used by Kunimoto & Matthews (2020). While this does, of course, change the exact values for M dwarf occurrence rates, due to the large errors on the values from Dressing & Charbonneau (2015) we believe our values for occurrence rates within the original bounds of this grid ($0.5\,R_\oplus \leq R_p \leq 4\,R_\oplus$, $0.5\,\mathrm{d} \leq P \leq 200\,\mathrm{d}$) are robust. As discussed in Section 3.7 we expect the yields of planets with periods between 200–400 d from *TESS* to be low and thus treat these bins as unconstrained with only an upper bound value. Furthermore we estimate values for planets between 4 and $16\,R_\oplus$ around M dwarfs using the values found for K dwarf stars by Kunimoto & Matthews (2020) but reduced by a factor of one-half to account for the expected lower occurrence rate of giant planets around M dwarfs (Sabotta et al. 2021; Bryant et al. 2023; Gan et al. 2023). To improve the accuracy of future yield estimations, it would be useful to constrain giant planet occurrence rates around M dwarfs as discussed in Bryant et al. (2023), Gan et al. (2023), and Sabotta et al. (2021). It is also worth noting that by rebinning the rates for M dwarfs we increase the shortest possible period of planet we simulate from 0.5 to 0.78 d, this means we are likely to underestimate yields in this region of period space as *TESS* has already found candidates (NASA Exoplanet Archive; Akeson et al. 2013) and nine confirmed planets (Vanderspek et al. 2019; Giacalone et al. 2022; Luque & Pallé 2022; Essack et al. 2023; Goffo et al. 2023) in this region.

5.6 Transit model

We use a trapezoidal model to approximate the shape of transits in our simulation as described in Section 2.2.2, this assumes a flat-bottomed shape to the transit and ignores the effects of limb-darkening (Espinoza & Jordán 2015, 2016; Agol et al. 2020) which may slightly increase the measured depth of a transit and thus increase SNR. However, we expect this effect to be small in magnitude and therefore did not use further computational resources to include it in our simulation. This may lead to our sensitivity values for *TESS* towards all exoplanets to be slightly conservative.

Additionally, this model assumes the contributions to SNR from Ingress and Egress are effectively half that of the full transit. This approximation works well enough for our purposes but use of the more accurate trapezoid model put forward in Kipping (2023) may improve our results. However, we expect the magnitude of this effect on our estimated SNR to be negligible.

While both of these effects are small, their inclusion in future iterations of TIARA could improve results, and may be worth including with more computational resources.

5.7 Probability of detection

As set out in Section 2.4, we use an incomplete gamma function to estimate the probability of detection in the TIARA simulation following Christiansen (2017), Hsu et al. (2019), and Kunimoto et al. (2022). As discussed in Kunimoto et al. (2022), there are some caveats associated with the use of this probability of detection function:

(i) *Kepler* monitored a different population of stars and had different light-curve properties to *TESS*. While our use of real *TESS* light curves allows us to account for many of the unique properties of *TESS* data we still are applying a probabilty of detection function developed for *Kepler* to a very different mission. It would be useful for work similar to that of Christiansen (2017) and Hsu et al. (2019) on *Kepler* DR25 to be performed on *TESS* to gain a more accurate understanding of the false positive rate and detection efficiency of *TESS*.

(ii) We perform a linear extrapolation for the detection efficiency of duotransit and monotransit events in *TESS*. While we believe the result to be reasonable as it produces the lower detection efficiency we expect for such events it is not based on the same rigorous testing done by Christiansen (2017) and Hsu et al. (2019) for three transit and greater events. Furthermore monotransits are often not found by the same algorithms that search for multitransit events and thus the probability of detection may not scale down linearly with number of transits down to the level of a monotransit. For this reason, it is also worth considering a simple $SNR \geq 20$ threshold for monotransits as discussed in Section 4.6.

Compared with *Kepler*, Vetting and confirmation of *TESS* candidates is easier at the same SNR due to the fact that *TESS* observes brighter stars and benefits from the *Gaia* data releases that better characterize host stars. Therefore it is likely that, with the caveats listed above, the use of the gamma function for *Kepler* on *TESS* data is likely to lead to more conservative (i.e. lower) estimates of sensitivity and therefore yield. However, quantifying the exact difference is difficult and therefore we continue to use the *Kepler* function.

Additionally, as shown in Section 4.6, the use of a gamma function, and SNR thresholds of 7.3 and 20 all recover a deficit in the number of long-period planets compared with the sample of TOI discoveries. This provides additional evidence for the potential of undiscovered long-period planets in *TESS* data.

5.8 Use of Years 1 and 3 SPOC FFI light curves

In our simulation, we use Years 1 and 3 SPOC FFI light curves which gives us a stellar population of ∼1.3 million stars in the Southern ecliptic hemisphere. This sample is selected in part due to computational limits of SPOC (Caldwell et al. 2020), and *TESS* observes many more stars at sufficient precision to detect transiting exoplanets. Thus, the total planetary yield from the *TESS* mission will be higher than those from just the SPOC FFI targets as we simulate here. However, the SPOC FFI sample prioritizes bright, main-sequence targets with low levels of dilution from other sources to fill the maximum of 160 000 targets per sector (Caldwell et al. 2020). The CTL (Stassun et al. 2019), as used by Kunimoto et al. (2022), uses a similar prioritisation metric but with a higher number of selected targets. This difference results in a smaller sample for SPOC, but with a greater proportion of targets most amenable to small planet detection. In future, it would be interesting to run TIARA

on a larger sample of light curves, such as those generated by the QLP (Huang et al. 2020).

6 SUMMARY AND CONCLUSIONS

We develop the TIARA pipeline to simulate the sensitivity of transit surveys to detecting transiting exoplanets. We focus in this paper on the Years 1 and 3 SPOC FFI sample from the *TESS* mission. In particular we are interested in the sensitivity and yield for longer-period planets that present as monotransits or biennial duotransits in the data. Our simulations is based on the actual stars monitored by *TESS* and the real *TESS* window functions (accounting for discontinuities in observations). We also use the actual noise properties of the light curves for each star.

We find a total of 2271^{+241}_{-138} exoplanets should be detected around AFGKM dwarf host stars in the Years 1 and 3 SPOC FFI light curves. Of these 403^{+64}_{-38} will have orbital periods greater than 25 d and 113^{+23}_{-17} will have orbital periods greater than 100 d. We find 4.4σ more predicted detections than the current TOI sample size of 1666. We find an increasing disparity between our predictions and actual *TESS* discoveries from the TOI catalogue at longer-periods, suggesting that the *TESS* discovery sample is incomplete at longer-periods and more long-period planets remain to be discovered in *TESS* data.

These additional planets will require concentrated follow-up efforts to confirm as the majority of them will be initially detected as some of the 215^{+37}_{-23} predicted *TESS* monotransits. 50 per cent of planet detections with periods above 25 d and 76 per cent of planet detections above 100 d will be monotransits. Aside from monotransits, a large portion of the remaining long-period planets will be found as biennial duotransit events with one transit in Year 1 and an additional in Year 3, with 113^{+22}_{-13} of these discoveries detected.

The TIARA pipeline developed for this project can be applied to additional *TESS* data sets such as the northern ecliptic SPOC FFI light curves from Years 2 and 4 and the recently released Year 5 SPOC FFI light curves. We intend to perform follow-up simulations using these additional SPOC data in the future. The QLP light curves (Huang et al. 2020) could also be analysed using TIARA. Reasonable assumptions of the observing strategy and current performance of *TESS* could also be used to create simulated light curves and make predictions of future *TESS* extended missions. With simulated data, TIARA can easily be used to predict the yields from future missions, in particular the upcoming *PLATO* (Rauer et al. 2014) mission.

ACKNOWLEDGEMENTS

DATA AVAILABILITY

The *TESS* data are accessible via the MAST portal at https://mast.stsci.edu/portal/Mashup/Clients/Mast/Portal.html. The binned sensitivity and yield maps used to produce Figs 6 and 7, and Figs A1 and B1 are available in a machine readable format from an open GITHUB repository at https://github.com/TobyRodel/TIaRA-TESS-Yields.

REFERENCES

Agol E., Luger R., Foreman-Mackey D., 2020, AJ, 159, 123
Aizawa M., Uehara S., Masuda K., Kawahara H., Suto Y., 2017, AJ, 153, 193
Akeson R. L. et al., 2013, PASP, 125, 989
Albrecht S. et al., 2012, ApJ, 757, 18
Ballard S., 2019, AJ, 157, 113
Barclay T., Pepper J., Quintana E. V., 2018, ApJS, 239, 2
Barnes J. W., Fortney J. J., 2004, ApJ, 616, 1193
Barnes J. W., O'Brien D. P., 2002, ApJ, 575, 1087
Bayliss D. et al., 2020, The Messenger, 181, 28
Benz W. et al., 2021, Exp. Astron., 51, 109
Bergsten G. J., Pascucci I., Hardegree-Ullman K. K., Fernandes R. B., Christiansen J. L., Mulders G. D., 2023, AJ, 166, 234
Borucki W. J. et al., 2010, Science, 327, 977
Bouma L. G., Winn J. N., Kosiarek J., McCullough P. R., 2017, preprint (arXiv:1705.08891)
Bryant E. M., Bayliss D., Van Eylen V., 2023, MNRAS
Caldwell D. A. et al., 2020, Res. Notes Am. Astron. Soc., 4, 201
Cassidy T. A., Mendez R., Arras P., Johnson R. E., Skrutskie M. F., 2009, ApJ, 704, 1341
Charbonneau D., Brown T. M., Noyes R. W., Gilliland R. L., 2002, ApJ, 568, 377
Christiansen J. L., 2017, in Haas M. R., Batalha N. M., eds, Planet Detection Metrics: Pixel-Level Transit Injection Tests of Pipeline Detection Efficiency for Data Release 25, Kepler Science Document KSCI-19110-001, id. 18. NASA Ames Research Center, Moffett Field, California
Christiansen J. L. et al., 2012, PASP, 124, 1279
Collier Cameron A. et al., 2006, MNRAS, 373, 799
Cooke B. F., Pollacco D., West R., McCormac J., Wheatley P. J., 2018, A&A, 619, A175
Cooke B. F., Pollacco D., Bayliss D., 2019, A&A, 631, A83
Dobos V., Charnoz S., Pál A., Roque-Bernard A., Szabó G. M., 2021, PASP, 133, 094401
Dong J. et al., 2021, ApJS, 255, 6
Dragomir D., Huang C. X., Kane S., Dalba P. A., Günther M. N., 2019, in AAS/Division for Extreme Solar Systems Abstracts. p. 103.04
Dragomir D. et al., 2023, in American Astronomical Society Meeting Abstracts. p. 318.03
Dressing C. D., Charbonneau D., 2013, ApJ, 767, 95
Dressing C. D., Charbonneau D., 2015, ApJ, 807, 45
Eberhardt J. et al., 2022, in Bulletin of the American Astronomical Society. p. 102.385
Espinoza N., Jordán A., 2015, MNRAS, 450, 1879
Espinoza N., Jordán A., 2016, MNRAS, 457, 3573
Essack Z. et al., 2023, AJ, 165, 47
Fressin F. et al., 2013, ApJ, 766, 81
Gaia Collaboration, 2016, A&A, 595, A1
Gaia Collaboration, 2018, A&A, 616, A1
Gaia Collaboration, 2023, A&A, 674, A1
Gan T. et al., 2023, AJ, 165, 17

Giacalone S. et al., 2022, AJ, 163, 99
Giles H. A. C. et al., 2018, A&A, 615, L13
Gill S. et al., 2020, ApJ, 898, L11
Goffo E. et al., 2023, ApJ, 955, L3
Grieves N. et al., 2022, A&A, 668, A29
Guerrero N. M. et al., 2021, ApJS, 254, 39
Harmanec P., 1988, Bull. Astron. Inst. Czechoslovakia, 39, 329
Hawthorn F. et al., 2024, TESS Duotransit Candidates from the Southern Ecliptic Hemisphere, MNRAS, 528, 2, 1841
Hilditch R. W., 2001, An Introduction to Close Binary Stars. Cambridge Univ. Press, Cambridge
Hippke M., Heller R., 2019, A&A, 623, A39
Howell S. B. et al., 2014, PASP, 126, 398
Hsu D. C., Ford E. B., Ragozzine D., Ashby K., 2019, AJ, 158, 109
Huang C., Wu Y., Triaud A. H. M. J., 2016, ApJ, 825, 98
Huang C. X. et al., 2018, preprint (arXiv:1807.11129)
Huang C. X. et al., 2020, Res. Notes Am. Astron. Soc., 4, 204
Jenkins J. M. et al., 2016, in Chiozzi G., Guzman J. C., eds, Proc. SPIE Conf. Ser. Vol. 9913, Software and Cyberinfrastructure for Astronomy IV. SPIE, Bellingham, p. 99133E
Johnson M., 2023, in American Astronomical Society Meeting Abstracts. p. 401.02
Johnson J. A., Aller K. M., Howard A. W., Crepp J. R., 2010, PASP, 122, 905
Kempton E. M. R. et al., 2018, PASP, 130, 114401
Kipping D. M., 2013, MNRAS, 434, L51
Kipping D., 2023, MNRAS, 523, 1182
Kipping D. M., Fossey S. J., Campanella G., 2009, MNRAS, 400, 398
Kovács G., Zucker S., Mazeh T., 2002, A&A, 391, 369
Kreidberg L., 2015, PASP, 127, 1161
Kreidberg L., 2018, in Deeg H. J., Belmonte J. A., eds, Handbook of Exoplanets. Springer International Publishing, Cham, p. 2083
Kruse E., Agol E., Luger R., Foreman-Mackey D., 2019, ApJS, 244, 11
Kunimoto M., Matthews J. M., 2020, AJ, 159, 248
Kunimoto M., Winn J., Ricker G. R., Vanderspek R. K., 2022, AJ, 163, 290
Lendl M. et al., 2020, MNRAS, 492, 1761
Luque R., Pallé E., 2022, Science, 377, 1211
Madhusudhan N., 2019, ARA&A, 57, 617
Madhusudhan N., Knutson H., Fortney J. J., Barman T., 2014a, in Beuther H., Klessen R. S., Dullemond C. P., Henning T., eds, Protostars and Planets VI. University of Arizona Press, Tucson, AZ, p. 739
Madhusudhan N., Amin M. A., Kennedy G. M., 2014b, ApJ, 794, L12
Makarov V. V., Efroimsky M., 2023, A&A, 672, A78
Maxted P. F. L., 2016, A&A, 591, A111
McLaughlin D., 1924, ApJ, 60 22
Muirhead P. S., Dressing C. D., Mann A. W., Rojas-Ayala B., Lépine S., Paegert M., De Lee N., Oelkers R., 2018, AJ, 155, 180
Mustill A. J., Davies M. B., Johansen A., 2017, MNRAS, 468, 3000
Öberg K. I., Murray-Clay R., Bergin E. A., 2011, ApJ, 743, L16
Osborn H. P. et al., 2023, MNRAS, 523, 3069
Owen J. E., 2019, Annu. Rev. Earth Planet. Sci., 47, 67
Pecaut M. J., Mamajek E. E., 2013, ApJS, 208, 9
Petrovich C., 2014, in AAS/Division for Planetary Sciences Meeting Abstracts #46. p. 301.03
Rauer H. et al., 2014, Exp. Astron., 38, 249
Rice M. et al., 2022, AJ, 164, 104
Ricker G. R. et al., 2014, in Oschmann J. M., Jr, Clampin M., Fazio G. G., MacEwen H. A., eds, Proc. SPIE Conf. Ser. Vol. 9143, Space Telescopes and Instrumentation 2014: Optical, Infrared, and Millimeter Wave. SPIE, Bellingham, p. 914320
Rossiter R., 1924, ApJ, 60 15
Sabotta S. et al., 2021, A&A, 653, A114
Simon A. E., Szabó G. M., Kiss L. L., Szatmáry K., 2012, MNRAS, 419, 164
Stassun K. G. et al., 2019, AJ, 158, 138
Sullivan P. W. et al., 2015, ApJ, 809, 77
Triaud A. H. M. J., 2018, in Deeg H. J., Belmonte J. A.eds,, Handbook of Exoplanets. Springer International Publishing, Cham, p. 1375
Tuson A. et al., 2023, MNRAS, 523, 3090
Ulmer-Moll S. et al., 2022, A&A, 666, A46
Ulmer-Moll S. et al., 2023, A&A, 674, A43
Valsecchi F., Rappaport S., Rasio F. A., Marchant P., Rogers L. A., 2015, ApJ, 813, 101
Van Eylen V., Albrecht S., 2015, ApJ, 808, 126
Vanderburg A. et al., 2015, ApJ, 800, 59
Vanderburg A. et al., 2016, ApJ, 827, L10
Vanderspek R. et al., 2019, ApJ, 871, L24
Villanueva S., Jr, Dragomir D., Gaudi B. S., 2019, AJ, 157, 84
Virtanen P. et al., 2020, Nat. Methods, 17, 261
Wheatley P. J. et al., 2018, MNRAS, 475, 4476
Winn J. N., 2014, in Seager S., eds, Exoplanets. University of Arizona Press, Tucson, AZ, p. 55
Wu Y., Lithwick Y., 2011, ApJ, 735, 109
Zhou G. et al., 2019, AJ, 158, 141
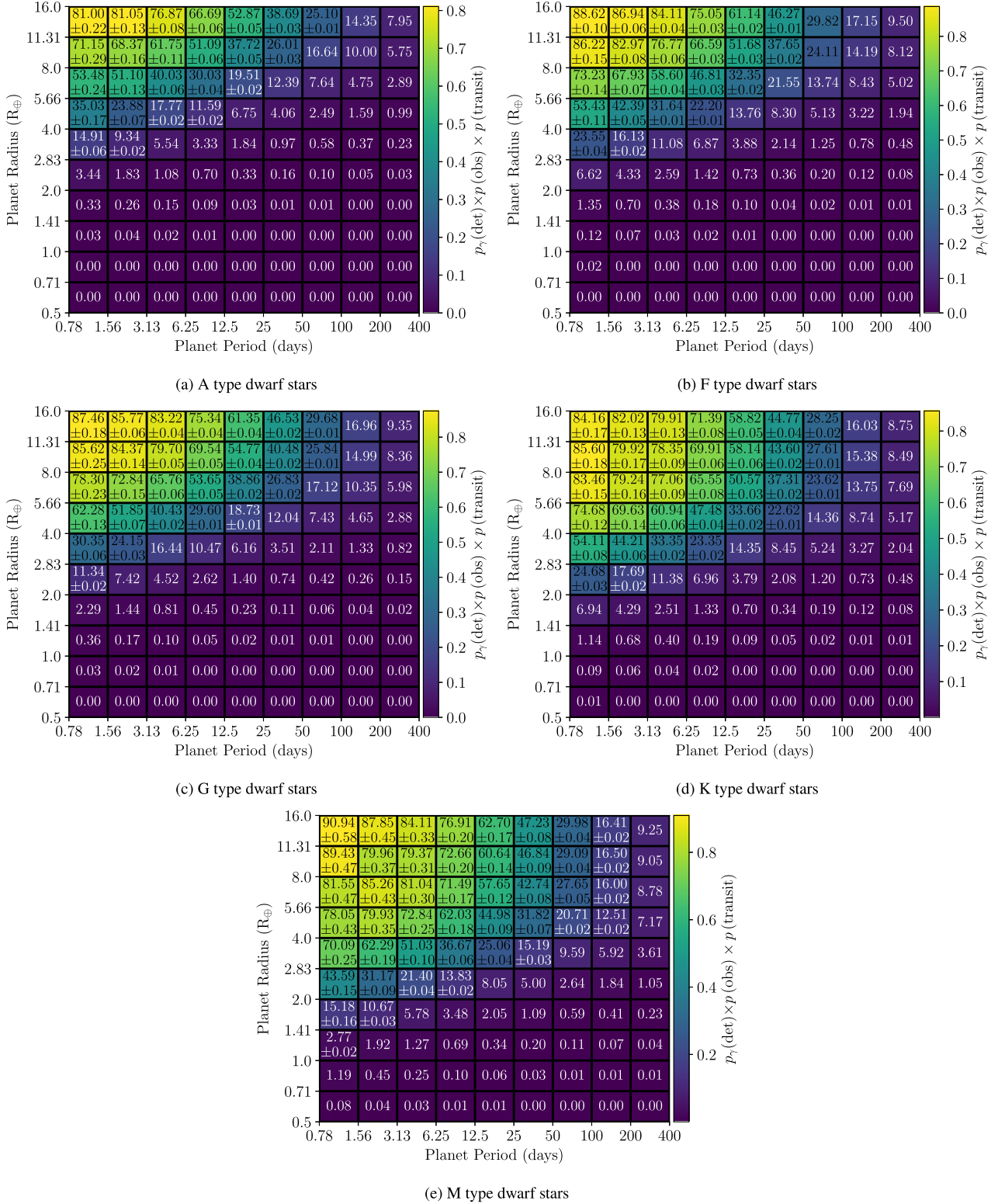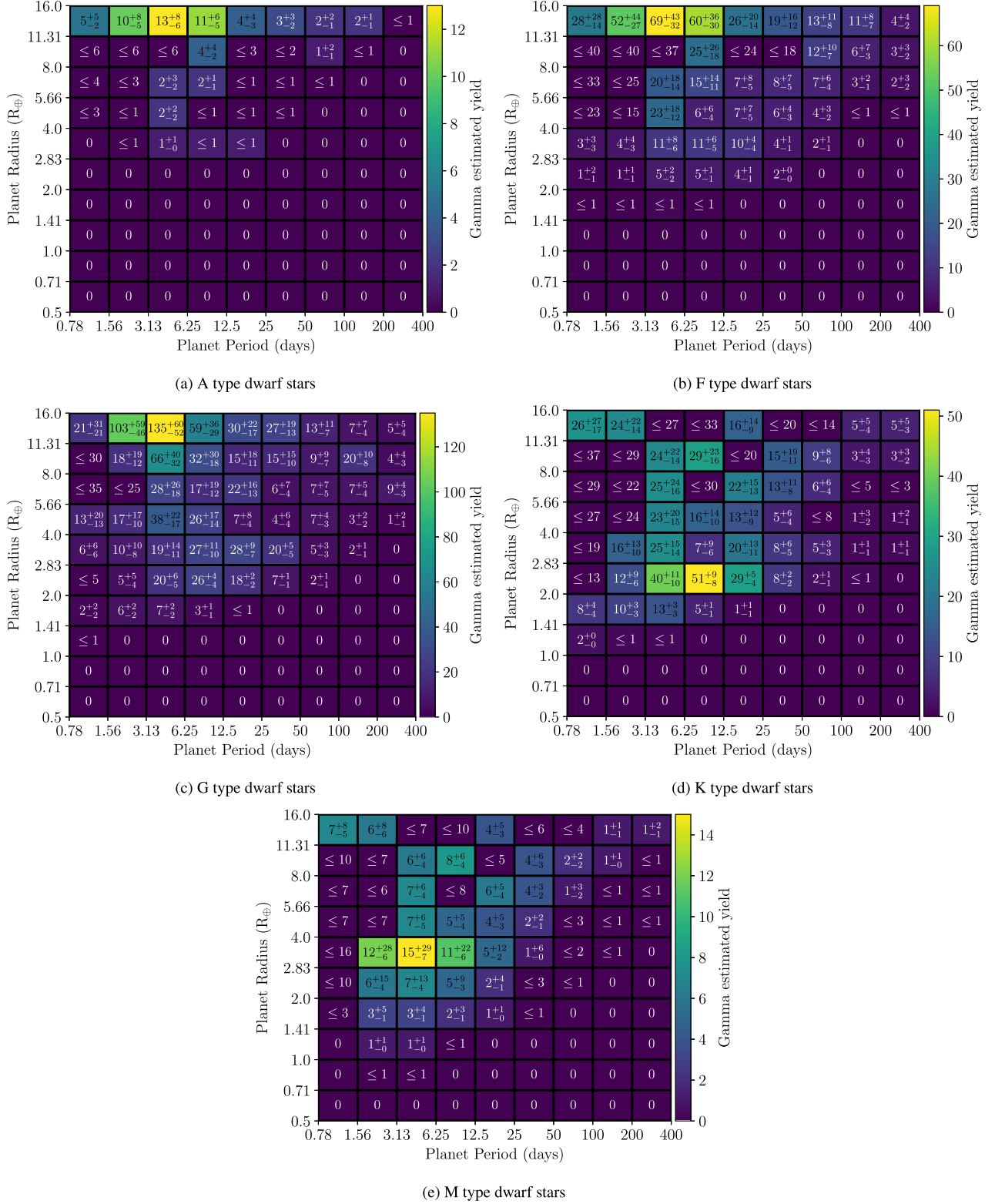
APPENDIX A: SENSITIVITY BY SPECTRAL TYPES

Figure A1. Sensitivity maps arranged by spectral type showing the probability of a transiting exoplanet being observed by *TESS* and then detected in the SPOC FFI ligh tcurves for Years 1 and 3. Numbers in each grid cell are the percentage sensitivity values. Where no uncertainties are given the uncertainty is 0 per cent to two decimal places.

APPENDIX B: YIELD BY SPECTRAL TYPE

(a) A type dwarf stars

(b) F type dwarf stars

(c) G type dwarf stars

(d) K type dwarf stars

(e) M type dwarf stars

Figure B1. Predicted yields of exoplanets from the Years 1 and 3 *TESS* SPOC FFI light curves divided by spectral type.

This paper has been typeset from a TeX/LaTeX file prepared by the author.